

## CFD MODELS OF MICROCEL AND JAMESON FLOTATION CELLS

P.T.L. KOH<sup>1</sup> and M.P. SCHWARZ<sup>1</sup>

<sup>1</sup> CSIRO Minerals, Clayton, Victoria 3169, AUSTRALIA

### ABSTRACT

Computational fluid dynamics (CFD) models of the Microcel column and Jameson cell have been developed for coal flotation. The models have been used to increase understanding of the cell hydrodynamics and to identify any opportunities to improve design and operation. The models incorporate micro-processes including particle-bubble attachments and detachments. From CFD simulations, liquid velocities, turbulent dissipation rates, gas hold-up, particle-bubble attachment rates and detachment rates are obtained. The attachment and detachment rates per particle have been used for comparing cell performance.

### NOMENCLATURE

$A_s$	constant = 0.5
$B$	buoyancy reduction force ( $\text{N m}^{-3}$ )
$Bo^*$	bond number
$C_l$	constant = 2
$d$	bubble or particle diameter (m)
$D_i$	diffusivity of phase I ( $\text{m}^2 \text{s}^{-1}$ )
$F$	drag force ( $\text{N m}^{-3}$ )
$g$	gravity vector ( $\text{m s}^{-2}$ )
$k$	turbulent kinetic energy ( $\text{m}^2 \text{s}^{-2}$ )
$k_l$	rate constant ( $\text{s}^{-1}$ )
$n$	particle number concentration ( $\text{m}^{-3}$ )
$P$	pressure or probability ( $\text{N m}^{-2}$ )
Re	Reynolds number
$S_i$	mass source or sink ( $\text{kg m}^{-3} \text{s}^{-1}$ )
$S$	surface ratio
$t$	time (s)
$U$	velocity ( $\text{m s}^{-1}$ )
$Z$	collision frequency ( $\text{m}^{-3} \text{s}^{-1}$ )
$\alpha$	volume fraction
$\beta$	bubble loading parameter
$\gamma$	shear rate ( $\text{s}^{-1}$ )
$\varepsilon$	turbulent eddy dissipation ( $\text{m}^2 \text{s}^{-3}$ )
$\theta$	contact angle (degree)
$\mu$	dynamic viscosity (Pa s)
$\nu$	kinematic viscosity ( $\text{m}^2 \text{s}^{-1}$ )
$\rho$	density ( $\text{kg m}^{-3}$ )
$\sigma$	surface tension ( $\text{N m}^{-1}$ )

### INTRODUCTION

Flotation is used by the minerals industry to separate valuable minerals from the ore in air-sparged flotation cells. Separation is achieved when particles of the valuable minerals preferentially attach to air bubbles and are floated to the surface, forming a froth layer. The particles are removed from the froth by means of an

overflow launder. The remaining slurry is discharged from the cell.

This paper describes an investigation using computational fluid dynamics (CFD) to increase understanding of the hydrodynamics in coal flotation and to identify any opportunities to improve the design and operation of both the Microcel column and Jameson cell. The flotation effect is included as three sub-processes involving collision, attachment and detachment. A turbulent collision model has been used (Koh *et al.*, 2000) to estimate the rate of particle-bubble encounters. The probability of collision is due to the streamline effect of fine particles moving around a larger bubble. The CSIRO CFD model incorporates micro-processes from cell hydrodynamics that affect particle-bubble attachments and detachments.

The issues facing coal flotation are two-fold: firstly, a drive to increase capacity of existing installations, and secondly, a need to increase the recovery of coarse coal. These issues are influenced by the flow conditions inside the cell. The conditions that affect coal recovery can be identified through an analysis of the CFD results in the tank. The effect of composite particles in coal flotation is considered by the spread of specific gravities and particle sizes. The application of CFD modelling can provide knowledge of the hydrodynamics involved in enhancing particle-bubble attachments while minimizing particle detachment from bubbles.

### MODEL DESCRIPTION

#### Transport Equations

Fundamental equations for the conservation of mass, momentum and turbulence quantities are solved. Using the Eulerian-Eulerian multi-fluid approach, the gas and pulp phases are treated as interpenetrating continua. The variables solved include Cartesian velocity components, pressure and volumetric fractions.

$$\frac{\partial(\alpha_i \rho_i)}{\partial t} + \nabla \cdot (\alpha_i \rho_i \vec{U}_i - \rho_i D_i \nabla \alpha_i) = S_i \quad (1)$$

$$\begin{aligned} \frac{\partial(\alpha_i \rho_i \vec{U}_i)}{\partial t} + \nabla \cdot (\alpha_i \rho_i \vec{U}_i \otimes \vec{U}_i) \\ = \nabla \cdot (\alpha_i (\mu_{L,i} + \mu_{T,i}) (\nabla \vec{U}_i + (\nabla \vec{U}_i)^T)) \\ + \alpha_i (B_i - \nabla P_i) + F_i + S_i \vec{U}_i \end{aligned} \quad (2)$$

The transport equations were solved within the computational fluid dynamics code CFX-4.4 (2001). The transport of solids within the pulp phase is modelled using the algebraic slip model. The source terms include the

pressure sources, the mass source or sink of gas entering and leaving the vessel, the generalised inter-phase force including drag and buoyancy forces.

Net attachment rate	$\frac{dn_{p1}}{dt} = -k_1 n_{p1} n_{bT} (1 - \beta) + k_2 n_{bT} \beta$
Attachment rate constant	$k_1 = Z_1 P_c P_a P_s$
Detachment rate constant	$k_2 = Z_2 (1 - P_s)$
Bubble loading	$\beta = \frac{n_{p2}}{S_{\max} n_{bT}}$ where $S_{\max} = 0.5S$ and $S = 4 \left( \frac{d_b}{d_p} \right)^2$
Collision frequency across eddies	$Z_1 = 5.0 \left( \frac{d_p + d_b}{2} \right)^2 \left( \overline{U_p^2} + \overline{U_b^2} \right)^{1/2}$
Critical diameter of particle or bubble	$d_i^2 > d_{crit}^2 = \frac{15 \mu_f \overline{U_f^2}}{\rho_i \varepsilon}$
Collision frequency within eddies	$Z_1 = \sqrt{\frac{8\pi}{15}} \left( \frac{d_p + d_b}{2} \right)^3 \left( \frac{\varepsilon}{\nu} \right)^{1/2}$
Turbulent fluctuating velocity of particle or bubble	$\sqrt{\overline{U_i^2}} = \frac{0.4 \varepsilon^{4/9} d_i^{7/9}}{\nu^{1/3}} \left( \frac{\rho_i - \rho_f}{\rho_f} \right)^{2/3}$
Detachment frequency	$Z_2 = \frac{\sqrt{C_1} \varepsilon^{1/3}}{(d_p + d_b)^{2/3}}$
Probability of collision	$P_c = \left( 1.5 + \frac{4}{15} \text{Re}_b^{0.72} \right) \frac{d_p^2}{d_b^2}$
Bubble Reynolds number	$\text{Re}_b = \frac{d_b \sqrt{\overline{U_b^2}}}{\nu}$
Probability of adhesion	$P_a = \sin^2 \left( 2 \arctan \exp \left[ \frac{-(45 + 8 \text{Re}_b^{0.72}) \sqrt{\overline{U_b^2}} t_{ind}}{15 d_b (d_b / d_p + 1)} \right] \right)$
Induction time	$t_{ind} = \frac{75}{\theta} d_p^{0.6}$
Probability of stabilisation	$P_s = 1 - \exp \left[ A_s \left( 1 - \frac{1}{Bo^*} \right) \right]$
Bond number	$Bo^* = \frac{d_i^2 \left[ \Delta \rho_{p,g} + 1.9 \rho_f \left( \frac{d_p}{2} + \frac{d_b}{2} \right) \right] + 1.5 d_i \left( \frac{4\sigma}{d_b} - d_i \rho_{p,g} \right) \sin \left( \pi - \frac{\theta}{2} \right)}{6\sigma \sin \left( \pi - \frac{\theta}{2} \right) \sin \left( \pi + \frac{\theta}{2} \right)}$

**Table 1:** Equations for particle-bubble interaction.

Turbulent kinetic energy  $k$  and turbulent dissipation rate  $\varepsilon$  are solved for the continuous pulp phase. The turbulent viscosity in the pulp phase is calculated using the standard  $k$ - $\varepsilon$  turbulence model (Launder and Spalding, 1974).

The flotation effect is simulated as three sub-processes involving collision, attachment and detachment. In simulations with flotation kinetics, the transfer of particles between the pulp and bubbles is achieved by applying source terms for particle number concentration  $n_i$  in the transport equation as follows:

$$\frac{\partial(\alpha_i n_i)}{\partial t} + \nabla \cdot (\alpha_i n_i \vec{U}_i) = -\phi_a + \phi_d \quad (3)$$

where  $\phi_a$  and  $\phi_d$  are sources or sinks specifying attachment and detachment rates respectively. The local particle-bubble detachment rates are from the flow field using equations shown in Table 1 (Koh and Schwarz, 2006).

## RESULTS

Multi-phase flow simulations (for liquid, air and solids) have been performed for the Microcel column and Jameson cell. Results of the simulations for both cells consist of velocity vectors, gas hold-up, turbulent dissipation rates and the particle-bubble attachment and detachment rates.

### Microcel Column

The Microcel flotation column of 4.9m diameter and 10.7m height operating with 12 spargers is manufactured by Eriez Pty Ltd. The CFD mesh of the column is shown in Figure 1. The hydrodynamics of the column operating with 250  $\mu\text{m}$  particles at 12% w/w solids and solid density of 1520  $\text{kg m}^{-3}$  are plotted in Figure 2 (velocity vectors) and Figure 3 (void fraction). An average bubble size of 1.0 mm is used in the simulation for the Microcel column (Filippov *et al*, 2000; Pyecha *et al*, 2006).

In Figure 2, there is a general circulating flow that rises in the centre with downward flow near the wall. An average circulating velocity of 1  $\text{m s}^{-1}$  for the pulp can be compared with a velocity of 5.4  $\text{m s}^{-1}$  at the sparger exits. Feed inlet velocity of 0.53  $\text{m s}^{-1}$  has some effect on the circulating flow creating complex flow patterns at the top of the column. The effect will be greater with increasing throughput and potentially can affect the pulp-froth interface.

In Figure 3, the contours of gas hold-up show a fairly uniform distribution of gas in the column with slightly higher hold-up near the wall due to the downward flow. An average void fraction of 0.176 for the whole column compares favourably with a value of 0.23 observed at the plant for the top part of the column, and a value of 0.35 predicted at the sparger exits.

In Figure 4, the turbulent dissipation rates are greatest near the sparger exits and near the two discharges. The turbulent dissipation rates near the pulp-froth interface are higher than values in the bulk because of the feed inlet flows and the presence of feed pipes and deflectors.

The distribution of attached particles is shown in Figure 5 where the higher concentrations are found in regions with higher gas hold-up. In Figure 6, the distribution of the unattached particles shows higher concentration at the base of the column, indicating some settling of unattached particles.

The attachment and detachment rates are plotted in Figure 7 and Figure 8 respectively. The maximum attachment rates occur at the centre of the column as well as near the feed and sparger exits, while the maximum detachment rates are found mainly near the sparger exits where the turbulent dissipation rates are highest. The local value of the turbulent dissipation rate has direct influence on the local particle-bubble detachment rate. It is important to identify the locations of these regions with high turbulent dissipation rates.

#### Jameson Cell

The standard B6000-20 Jameson cell, manufactured by Xstrata Technology, has a diameter of 6m operating with 20 downcomers. The CFD mesh is shown in Figure 9 consisting of the pulp and froth zones with a bubble disperser plate.

CFD simulation has been performed for the case with 7.5% w/w solids, 250  $\mu\text{m}$  size and solid density 1520  $\text{kg m}^{-3}$ . In Figure 10, the general pattern of flow from the downcomer exit to the pulp-froth interface is around the bubble disperser with a small portion of flow through the perforated plate. The pulp-air mixture has a velocity of 0.49  $\text{m s}^{-1}$  with a void fraction of 0.43 at the downcomer exits. The velocities at the inner launder wall tend to be higher than those at the outer launder wall. The direction of velocities at the inner launder wall is downward at the deeper end, but it is upward at the shallow end. This is due to the high gas hold-up beneath the inner launder, as shown in Figure 11. Because of the sloping wall, the air escapes towards the shallow end of the launder. The average void fraction in the cell is 0.072, while in the upper part of the cell, the value is about 0.16.

In Figure 12, the turbulent dissipation rates are highest near the inner launder wall where the flow is influenced by the air coming out beneath the sloping launder wall. Because of this effect, the turbulent dissipation rates at the pulp-froth interface are also higher towards the inner launder.

In Figure 13, the distribution of the unattached particles shows higher concentration at the base of the cell, indicating some settling of unattached particles. The distribution of attached particles is shown in Figure 14 where the higher concentrations are found in regions with higher gas hold-up. In the simulation, 80% of the particles were assumed to be attached to the bubbles at the exit of the downcomers based on data by Harbort et al (2006).

The attachment and detachment rates are plotted in Figure 15 and Figure 16 respectively. The maximum attachment rates occur near the downcomer exits while the maximum detachment rates are found near the wall of the inner launder where the turbulent dissipation rates are highest. Thus, it is important to minimise these regions with high turbulent dissipation rates to minimise detachment.

## CONCLUSION

CFD simulations for both the Microcel column and Jameson cell have produced data that provide useful insights in relating cell hydrodynamics to the particle-bubble attachment and detachment rates for coal flotation. It has been found that the local value of the turbulent dissipation rate has a direct influence on the local particle-bubble detachment rate. It is therefore important to identify the locations of these regions with high turbulent dissipation rates.

Under the conditions investigated, the Microcel column is well designed with fairly good performance throughout the column, but further improvements are still possible. In the Jameson cell, the turbulent dissipation rates were found to be greatest near the inner launder where the flow is influenced by the air coming from beneath the sloping launder wall. Because of this effect, the turbulent dissipation rates at the pulp-froth interface are also higher near the inner launder. Cell performance can be improved with further investigations.

This work has demonstrated that CFD modelling is a cost effective means of developing an understanding of particle-bubble attachments and detachments, and can be used to identify and test potential cell or process modifications.

## ACKNOWLEDGEMENT

The authors are grateful to the Australian Coal Association Research Program (ACARP) for financial support and permission to publish. Thanks are also presented to Xstrata Technology Pty. Ltd. and Eriez Magnetics Pty. Ltd. for supplying drawings of the flotation cells.

## REFERENCES

- CFX User Guide, Release 4.4*, (2001), Computational Fluid Dynamics Services, AEA Industrial Technology, Harwell Laboratory, Oxfordshire, UK.
- FILIPPOV, L.O., JOUSSEMET, R. and HOUOT, R., (2000) "Bubble spargers in column flotation: Adaption to precipitate flotation", *Minerals Engineering*, **13**, 37-51.
- HARBORT, G.J., COWBURN, J.A. and MANLAPIG, E.V., (2005) "The effect of residence time and aeration on coal recovery within the high intensity zone of a flotation machine", Centenary of Flotation Symposium, Brisbane, p. 449-456.
- KOH, P.T.L., MANICKAM M. and SCHWARZ, M.P., (2000) "CFD Simulation of Particle-bubble Collisions in Mineral Flotation Cells", *Minerals Engineering*, **13**, 1455-1463.
- KOH, P.T.L. and SCHWARZ, M.P., (2006) "CFD Modelling of Particle-bubble Attachments in Flotation Cells", *Minerals Engineering*, **19**, No. 6-9, 619-626.
- LAUNDER, B.E. and SPALDING, D.B., (1974) The numerical computation of turbulent flows. *Comp. Meths. Appl. Mech. Engng.*, **3**, 269-289.
- PYECHA, J., LACOUTURE, B., SIMS, S., HOPE, G. and STRADLING A., (2006) "Evaluation of a Microcel sparger in the Red Dog column flotation cells", *Minerals Engineering*, **19**, 748-757.

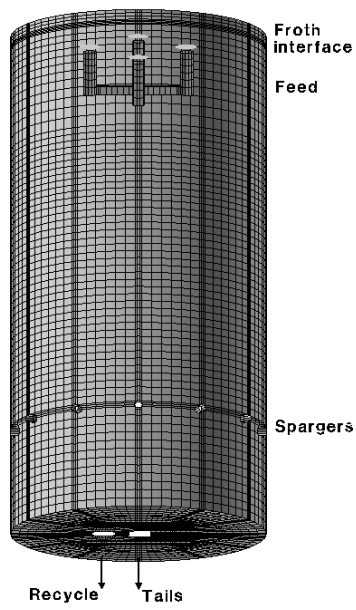


**Figure 1:** CFD mesh of Microcel column.

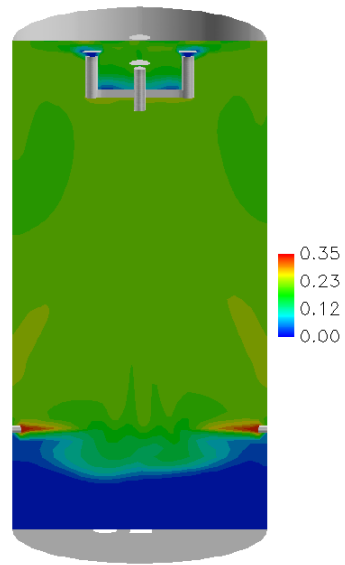


**Figure 3:** Void fraction in Microcel column.

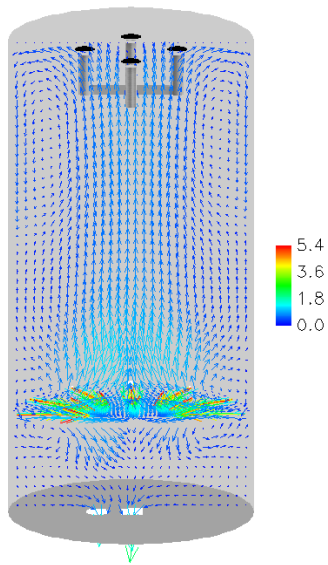


**Figure 2:** Liquid velocity ( $\text{m s}^{-1}$ ) in Microcel column.

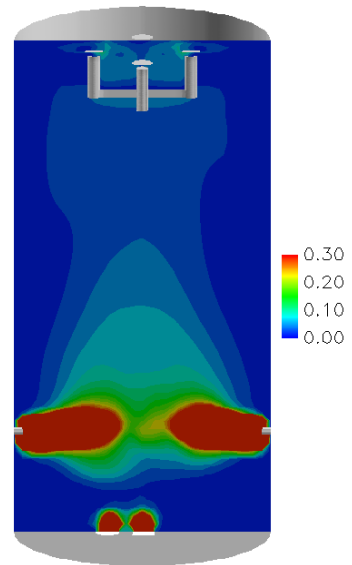


**Figure 4:** Turbulent dissipation rate ( $\text{W kg}^{-1}$ ) in Microcel column.

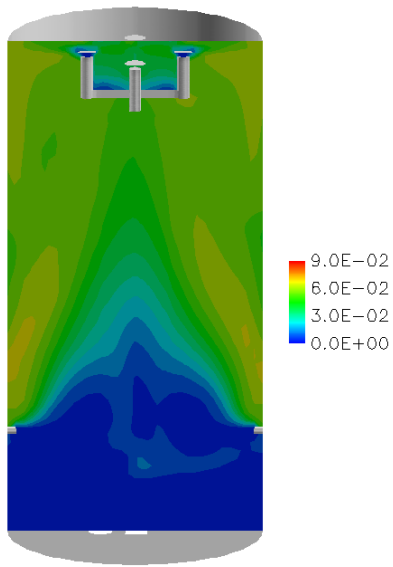


**Figure 5:** Attached particle-volume fraction in Microcel column.

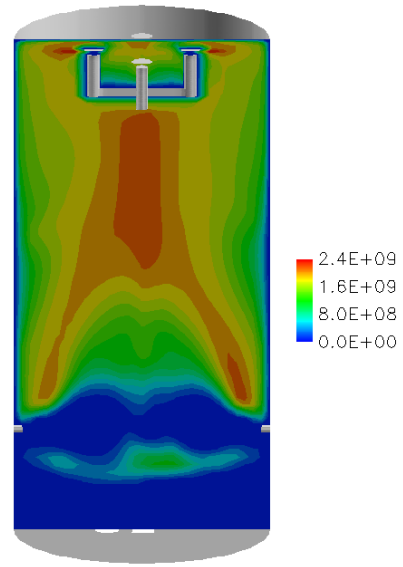


**Figure 7:** Attachment rate ( $\text{m}^{-3} \text{s}^{-1}$ ) in Microcel column.

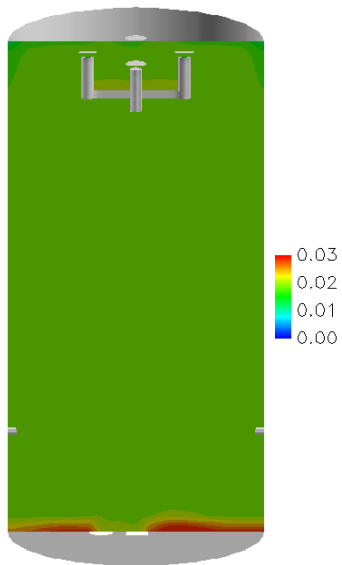


**Figure 6:** Unattached particle-volume fraction in Microcel column.

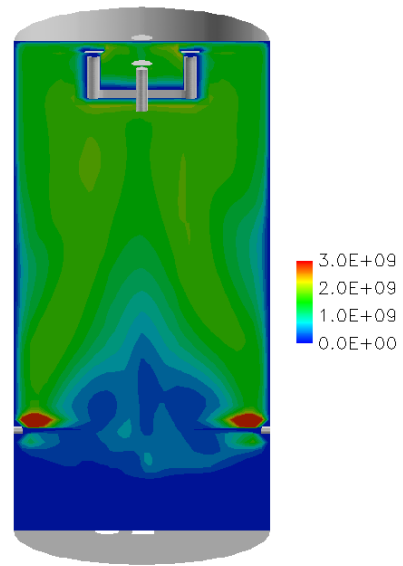


**Figure 8:** Detachment rate ( $\text{m}^{-3} \text{s}^{-1}$ ) in Microcel column.

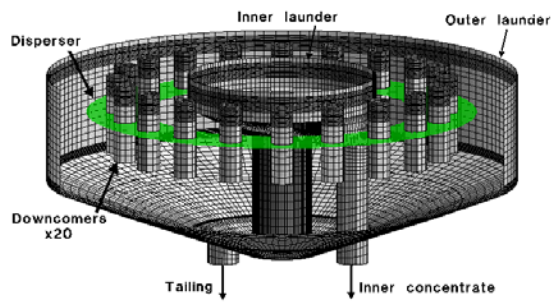


**Figure 9:** CFD mesh of Jameson cell with twenty downcomers.

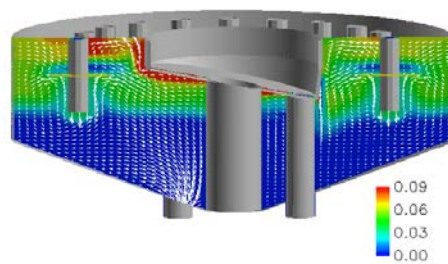


**Figure 13:** Attached particle-volume fraction in Jameson cell.

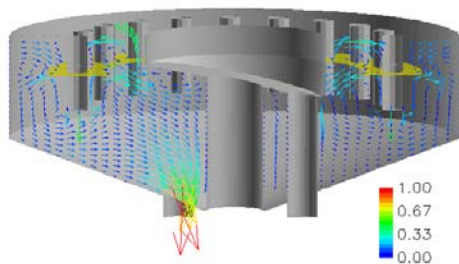


**Figure 10:** Liquid velocity ( $\text{m s}^{-1}$ ) in Jameson cell.

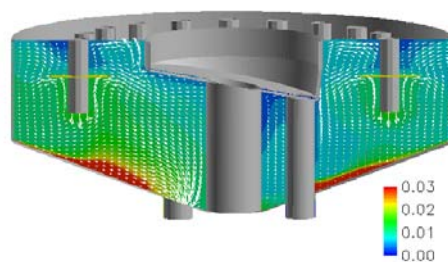


**Figure 14:** Unattached particle-volume fraction in Jameson cell.

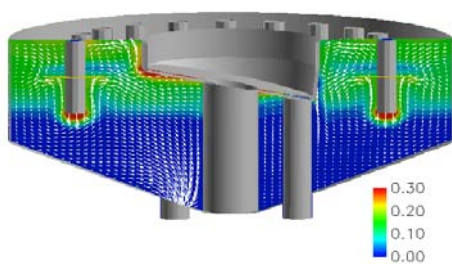


**Figure 11:** Void fraction in Jameson cell.

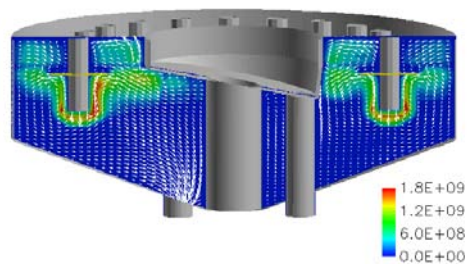


**Figure 15:** Attachment rate ( $\text{m}^{-3} \text{s}^{-1}$ ) in Jameson cell.

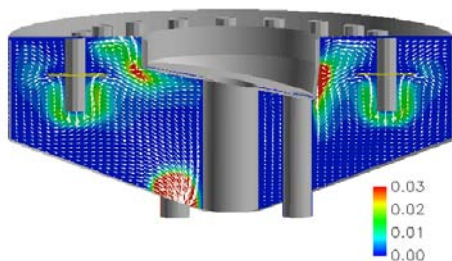


**Figure 12:** Turbulent dissipation rate ( $\text{W kg}^{-1}$ ) in Jameson cell.

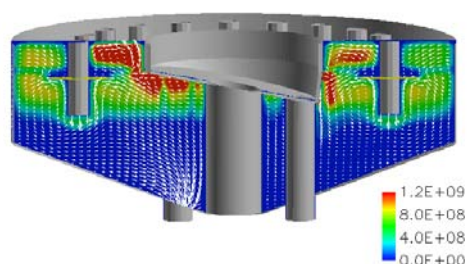


**Figure 16:** Detachment rate ( $\text{m}^{-3} \text{s}^{-1}$ ) in Jameson cell.